Post-Optimality Pareto-Robustness Analysis of an Earth-Observation Satellite Mission

Postoptimality Pareto-Robustness Analysis of an Earth-Observation Satellite Mission

G. Ridolfi*
Politecnico di Torino, 10129 Torino, Italy
E. Mooij†
Delft University of Technology, 2629 HS Delft, The Netherlands
and
S. Corpino‡
Politecnico di Torino, 10129 Torino, Italy

In this paper, a methodology for postoptimality studies to assess the robustness of the Pareto-optimal solutions computed with a multi-objective optimization algorithm is presented. The proposed Pareto-robust optimization approach is based on factorial design for sampling the design region in the neighborhood of the Pareto-optimal solutions. It allows for estimating a metric for the Pareto robustness and contributes to improving convergence of the known Pareto-front toward the true Pareto front. Further, sensitivity analysis of the performance and response surfaces in the neighborhood of the optimal solutions are computed without additional computational cost. The proposed approach is applied to two validation test cases and to the design of a satellite Earth-observation mission for disaster monitoring. The results show that the Pareto-robust optimization approach can correctly detect Pareto-robust solutions on the Pareto front, and that it provides additional Pareto-optimal solutions at the same time, eventually improving the original known Pareto front. In the case of the Earth-observation mission, the study demonstrates the possibility to enable and promote tradeoffs among the engineering team members to obtain an effective decision-making process. The solution identified as the most Pareto-robust one can be considered quite uncommon but still very reasonable due to the assumptions, presenting a satellite in a nonsun-synchronous medium Earth orbit.

Nomenclature

D	=	aperture diameter of the optical instrument, m
$d(\cdot,\cdot)$	=	Euclidean distance operator
$E(\cdot)$	=	expected value operator
$\mathbf{f}(\mathbf{x})$	=	vector of the objective functions
g	=	inequality constraint
h	=	equality constraint
$\mathbf{h}$	=	satellite altitude above the Nadir point, m
PF	=	Pareto front
PR	=	Pareto robustness
S_i	=	sensitivity index of the regression-model factor
$V(\cdot)$	=	variance operator
$\mathbf{x}$	=	design vector
X_{nadir}	=	ground spatial resolution at satellite Nadir, m
x_i	=	design variable i
$\mathbf{x}_{-i}$	=	design vector without the design variable x_i
Y	=	response of the regression model
$\beta_i, \beta_{ij}, \beta_{ii}$	=	regression coefficients
λ	=	radiation wavelength, m
χ	=	design space
$\mathcal{F}$	=	objective space
Ψ	=	degree of constraint violation

I. Introduction

IN THE last decades, the task of designing space systems has experienced a trend of increasing complexity. This is mainly caused by the demand for development time and cost reduction, while maintaining high quality standards. One of the main objectives during the design is to set the levels of design factors (variables) such that the performances of interest (i.e., the objectives) are optimized, the requirements are met, and the constraints are not violated. Generally speaking, the design factors can be either continuous or discrete.

Many techniques have been developed that could, in principle, be used to solve a multi-objective, constrained, and potentially discontinuous optimization problem, providing solutions in the form of Pareto fronts (PF) [1–7]. Even though it is empirically proven that excellent results can be obtained using them, several authors recognize the importance of performing postoptimality studies to locally improve the results [6–9].

In this paper, a novel approach for postoptimality studies applied to complex-system design is presented. It is based on a particular implementation of factorial design to locally improve the Pareto-optimal solutions, computed with a multi-objective optimization technique. This enables the possibility of finding better solutions in the case of unsatisfactory convergence and providing information on the Pareto-robustness of the Pareto-optimal solutions.

The main objectives are to obtain an improved Pareto front, and to provide the design team with a means to rank the optimal solutions based on their Pareto robustness PR. The PR metric introduced in this paper allows for ranking the solutions on the Pareto front according to their robustness to design-variable dispersion and/or modification. The PR enables the possibility to identify new and possibly more suitable alternatives that would not have been discovered otherwise.

As will be demonstrated later in the paper, the simulations required to determine the PR are also used to support the tradeoff process, computing the main effects of and interactions between the design variables. This can potentially aid in early discovery of dominating phenomena in the problem of interest, thus efficiently steering the decisions of the design team.

To illustrate the proposed approach, it will be applied to two validation test cases and to a case study of an Earth-observation satellite for crisis management in the case of natural disasters. The satellite system includes mathematical models of the satellite subsystems and payload, as well as models of potential launchers, ground segment, and a mission propagator.

The remaining part of the paper is organized as follows. In Sec. II, the details of the Pareto-robust optimization approach (PROA) are provided. Section III gives a description of the case study in terms of mathematical models, objectives, and constraints. In Sec. IV, the results of the simulations are discussed. Section V concludes the paper with some final remarks. In the Appendix, the validation test cases are presented, and the results obtained using PROA are discussed.

II. Pareto-Robust Optimization Approach

A. Origins of Pareto-Robust Optimization Approach

The problem of designing and optimizing a space system, considering its operative environment and the mission it will accomplish, is highly constrained and characterized by having multiple objectives, with continuous and discrete (e.g., architectural) variables.

In multi-objective optimization problems the "optimum" is treated differently compared with single-objective optimization problems. The former aims at finding a set of good compromises, i.e., tradeoffs, rather than a single optimal solution, by optimizing all the objectives simultaneously. This set of solutions is found using the Pareto-optimality concept. A solution is defined to be Pareto-optimal or *nondominated* if there is no feasible solution for which one cannot improve a single objective without causing a degradation of at least one other objective. According to the Pareto-optimality concept, a vector $\mathbf{a} \in X$ is said to dominate another vector $\mathbf{b} \in X$ in a minimization problem, also written as $\mathbf{a} \prec \mathbf{b}$, if and only if the following relationship holds:

$$\forall\, i \in \{1, \ldots, N\}:\ f_i(\mathbf{a}) \leq f_i(\mathbf{b}) \wedge \exists j \in \{1, \ldots, N\}:\ f_j(\mathbf{a}) < f_j(\mathbf{b}) \tag{1}$$

The set of nondominated vectors plotted in the objective space is defined as the Pareto front. The determination of the true Pareto front PF_{true} (i.e., the theoretical obtainable Pareto front), depends on many aspects such as the complexity of the problem of interest, the number of design variables and objectives, the nature of the front itself (concave/convex, continuous/discrete), and the number of function evaluations executed. In real-life applications PF_{true} is almost never reached, especially due to computational limitations and problem complexity, as demonstrated in [8,9].

Therefore, many authors working with global multi-objective algorithms suggest that a local analysis should be performed for the solutions belonging to the Pareto front, [4,6,7]. The main reason is that, for instance, some of the multi-objective optimization algorithms (like evolutionary algorithms) do not guarantee convergence to the optimum, even though it is empirically proven that they can provide excellent results. The front obtained with a multi-objective optimization algorithm is usually referred to as PF_{known}. It represents the best approximation of PF_{known} computed by the algorithm. Postoptimality studies should therefore be performed to improve convergence of PF_{known} toward PF_{known}.

Moreover, from an engineering point of view not all optima are equal, not even those on the Pareto front. Some optima could be the result of a particular combination of design variables that will exhibit a steep drop in performance when the levels of these variables are only slightly modified. Especially during preliminary design of space systems, the design variables are only frozen after several design iterations. Thus, there is a risk that the selected design baseline may suffer from performance degradation in subsequent phases of the design cycle. In this sense, a more Pareto-robust solution can be considered a less risky one.

Further, the determination of the sensitivity of the optimal (preferably also Pareto-robust) solutions and the shape of the design

space around it is considered to be of prime importance for the design team to perform more informed tradeoffs. In separate research, we propose a regression-based approach for the computation of global sensitivity analysis and response surfaces at a reduced computational effort if compared with Monte Carlo techniques [10,11]. The approach is based on sampling according to the central composite design (CCD).

The CCD is a typical factorial design used to determine first- and second-order factor effects on the objectives, as well as interactions between the design variables. The second-order model considered in this discussion is given by

$$Y = \beta_0 + \sum_{i=1}^{k} \beta_i x_i + \sum_{i=1}^{k} \beta_{ii} x_i^2 + \sum_{i=1}^{k-1} \sum_{j=i+1}^{k} \beta_{ij} x_i x_j \qquad (2)$$

Here, β_i, β_{ii} and β_{ij} are the so-called regression coefficients that are calculated by fitting the surface through the design points determined by the CCD. In Sec. II.C we show how to compute sensitivity indices from Eq. (2) using CCD sampling.

The main advantage of using sensitivity analysis at this stage is that the factors that affect the variance of the objectives the most can be identified before actually computing the response surfaces, via regression analysis. This reduces the information provided to the design team that can focus on fewer response surfaces computed with the most relevant factors as independent variables.

Summarizing, the proposed approach for postoptimality studies can be used to assess the robustness of the Pareto-optimal solutions, computed with a multi-objective optimization algorithm, and contributes to improving convergence of PF_{known} toward PF_{true}. At the same time it provides graphical information regarding sensitivity and design-space shape to the design team.

B. Multi-Objective Global Optimization

Many multi-objective optimization techniques and algorithms have been developed and implemented to solve ad hoc mathematical problems, see for example [5–7].

In general, global optimization algorithms are preferred over local gradient-based techniques, mainly because the latter require continuity in the search space of objective functions and constraints and their first derivatives. Especially when dealing with architectures of a space system, the design variables are not always continuous, e.g., the choice of a particular launcher. Further, such methods are characterized by finding local optima rather than global.

Global optimization methods may cover a large portion of the design space while searching for the optimum, and provide mechanisms for avoiding local optima, e.g., random mutation in the case of genetic algorithms [3]. Deterministic methods like branch-and-bound algorithms [1,12], relaxation strategies, enumerative methods [1], and interval-analysis methods show poor convergence in some cases and a rapid increase of computational effort when the dimensions of the search space increase [13]. Dynamic programming (DP) is a combinatorial optimization technique, which demonstrated to reach exact solutions for problems with specific formulations (also multi-objective [14]).The DP technique uses solutions of

subproblems, of similar nature to the main problem to optimize, to build the global optimal solution [15]. The modification of the problem structure to be solvable by a DP algorithm is not always a feasible alternative, especially in collaborative, possibly distributed design environments.

Classical methods (stochastic or deterministic) for the generation of the Pareto front, such as the normal boundary intersection [16], the adaptive weighted sum [17], the direct search domain [18], and the normal constraint method [19], to mention a few, have shown good performance in finding Pareto-optimal solutions for multi-objective, constrained, continuous and discontinuous optimization problems. A good overview of these methods and a comparison of the performance of a few of them are presented in [5].

The nonclassical heuristic methods, such as evolutionary strategies [2], simulated annealing [20], and tabu-search [21,22], proved to be particularly flexible and applicable to continuous and discontinuous problems with one or more objectives and constraints [6,7]. Heuristic algorithms also demonstrated a high degree of scalability [23,24]. However, in general this comes at the price of inexact solutions, which justifies the need for postoptimality studies. Also, other approaches exist that exploit alternative formulations of the multi-objective problem. The iso-performance method, for instance, allows for obtaining optimal solutions amongst those that were previously determined to meet the performance requirements with sufficient margins [25]. Physical programming [26] instead demonstrated the possibility to generate PF in multi-objective problems considering experts judgment already during the optimization. Well-distributed PF of physically meaningful solutions were obtained.

All of the global optimization methods discussed so far have advantages and disadvantages depending on the problem to be solved. However, they all provide a Pareto front as a result. The PROA proposed in this paper can in principle be implemented considering a Pareto front obtained by any Pareto-generating technique. As will be demonstrated later, Pareto robustness is based on the dominance principle, which is a general concept independent from any specific optimization algorithm.

For the specific test cases used in this paper, we decided to use a heuristic multi-objective optimization algorithm, the nondominated sorting genetic algorithm II (NSGAII) [27]. It is a very popular algorithm, for which many versions have been implemented and released by the developers, and for which extensive tests on a wide range of multi-objective problems have been performed, see for instance [5,28,29].

C. Pareto-Robust Optimization Approach

Once the Pareto front of the optimization problem has been obtained, PROA can be executed on the solutions of the PF_{known}. In PROA, the central point of the local CCD represents the design vector corresponding to a single point on PF_{known}. The other points are derived in all dimensions by scattering the design-variable levels on the basis of a certain percentage of the variability ranges (usually 5–10%). This percentage shall be carefully selected by the design team, on the basis of the accepted range of design-variable variation within which degradation of the performances is expected, or not.

For each solution of PF_{known}, the design vectors of the local CCD are evaluated, and the Pareto-robustness is computed. The concept of Pareto-robustness is explained in terms of Euclidean distance of the design vectors in objective space, taking constraints into account. In an M-dimensional space the Euclidean distance between two vectors $\mathbf{a} = [a_1, a_2, \ldots, a_M]$ and $\mathbf{b} = [b_1, b_2, \ldots, b_M]$ can be computed with the following expression:

$$d(\mathbf{a}, \mathbf{b}) = \sqrt{\sum_{i=1}^{M} (a_i - b_i)^2} \tag{3}$$

In Fig. 1 a two-dimensional schematic representation of the rule used to compute the Euclidean distance to PF_{known} is shown. The rule is implemented considering a nondimensional objective space and PF_{known}. If a CCD-generated vector is nondominated, then the Euclidean distance between that vector and the closest Pareto-optimal solution is computed, as in the case of P_1-S_1 and P_2-S_2 of Fig. 1. The closest Pareto-optimal solution is now determined between the vector of interest and all the Pareto-optimal solutions. In case a CCD-generated vector is dominated, instead, the M closest Pareto-optimal solutions to the vector of interest are determined as a first step. In Fig. 1, for instance, P_2 and P_3 represent the closest Pareto-optimal solutions to D_1, D_2, and D_3. The distance from the PF_{known} is then computed using Eq. (3) in the improving direction of each single objective toward the local nadir points. The local nadir points are the vectors made of the upper bounds of each objective, restricted to the M Pareto-optimal solutions $N_k = [\max(P_I(f_1), P_{II}(f_1), \ldots, P_M(f_1)), \ldots, \max(P_I(f_M), P_{II}(f_M), \ldots, P_M(f_M))]$, where $P(f_i)$ is the ith dimension (i.e., the ith objective) of the vector $\mathbf{P}$ and $[P_I, P_{II}, \ldots, P_M]$ are the M closest Pareto-optimal solutions to a certain CCD-generated vector D_i. The Euclidean distance is computed for each nondominated CCD-generated vector D_i iteratively, adding a contribution to the distance considering one dimension at a time. For each objective f_j, with $j = [1, 2, \ldots, M]$, a contribution is added according to the following rule:

$$d(D_i, PF_{known}) = d(D_i, PF_{known}) + \begin{cases} [D_i(f_j) - N_k(f_j)]^2 \text{ if } D_i(f_j) > N_k(f_j) \\ 0 \qquad\qquad\qquad \text{Otherwise} \end{cases} \tag{4}$$

Once the contribution from all the dimensions have been added, the square root of $d(D_i, PF_{known})$ is taken as the final value for the Euclidean distance between D_i and PF_{known}.

Following this rule, for instance, the distances of D_1, D_2, and D_3 from PF_{known} are computed as follows (Fig. 1):

$$d(D_1, PF_{known}) = \sqrt{0 + [D_1(f_2) - \max(P_2(f_2), P_3(f_2))]^2} \tag{4a}$$

$$d(D_2, \mathrm{PF}_{\mathrm{known}}) = \sqrt{\begin{array}{c}[D_2(f_1) - \max(P_2(f_1), P_3(f_1))]^2 \\ +[D_2(f_2) - \max(P_2(f_2), P_3(f_2))]^2\end{array}} \quad (4b)$$

$$d(D_3, \mathrm{PF}_{\mathrm{known}}) = \sqrt{[D_3(f_1) - \max(P_2(f_1), P_3(f_1))]^2 + 0} \quad (4c)$$

The distance d of nondominated solutions to $\mathrm{PF}_{\mathrm{known}}$ is considered to be negative to prefer design regions in which $\mathrm{PF}_{\mathrm{known}}$ can be improved. Further, for each CCD-generated design vector the degree of constraint violation Ψ is added to the distance computed with Eq. (4) to penalize design regions that may generate infeasible solutions. Ψ is computed for constraints in both the nondimensional design and objective space, and is equal to the amount by which the constraint is violated.

The Pareto robustness figure of merit is thus computed taking into account two contributions, namely the Euclidean distance from $\mathrm{PF}_{\mathrm{konwn}}$ and the degree of constraint violation Ψ of all the CCD points:

$$\mathrm{PR} = \sum_{j=1}^{N_{\mathrm{CCD}}} (d(\mathbf{a}_j, \mathrm{PF}_{\mathrm{known}}) + \Psi_j) \quad (5)$$

where N_{CCD} is the number of CCD-generated design vectors. In Fig. 2, a schematic of the Pareto robustness concept is shown, using a two-dimensional design space and a two-dimensional objective space. The Pareto-optimal solutions D and E found during the global optimization phase are analyzed using a CCD. Each CCD point in the design space corresponds with a point in objective space. PROA searches for those solutions on $\mathrm{PF}_{\mathrm{known}}$ that give close-to-optimal, Pareto-improving, and constraint-meeting solutions when design-variable levels are perturbed from the original Pareto-optimal point.

There can be cases in which the central point of the CCD in the design space must be moved before executing the simulations, to avoid exceeding the boundaries of the design variables (see Fig. 2, solution E). Shifting the CCD still allows for determining the robustness of roughly the same design region and includes the original Pareto-optimum solution.

The statistical variance of the objectives in the objective space could also be used as an indication of the variability of the objectives with respect to the nominal value. Indeed, statistical mean and variance are sometimes used in the literature with this purpose, see for instance [30,31]. The main drawback of the direct use of statistical mean and variance is that, from a Pareto perspective, it may result in misleading indications. Consider again the schematic example of Fig. 2. The statistical variance of the data generated by computing a CCD around solutions D and E is the same (see the shadowed ellipses). However, the Pareto-robustness of solution E is much higher than the Pareto-robustness of solution D. This is indicated by the smaller distances of the design points from $\mathrm{PF}_{\mathrm{known}}$, by the

fact that the constraints are never violated, and by the fact that three solutions (i.e., the square symbols) are better than these on PF_{known} de facto pushing PF_{known} toward PF_{true}.

At this stage of PROA an improved Pareto front may have been obtained, and all optimal solutions have been ranked according to their Pareto robustness. The risk of obtaining far-from-optimal solutions in case of uncertainty (programmatic or technical) in the determination of the design variables is mitigated if the design team decides to steer for the more Pareto-robust areas of the design space.

To better support its decision and to provide more insight in the system behavior in one particular region of the design space (most likely regions with a high Pareto-robustness ranking), the data coming from the CCD analysis of the selected solution are reused to compute the sensitivity analysis based on the variance of the performance. In particular, the variance is decomposed in the contribution of all the terms of the model represented by Eq. (2), using the sensitivity indices [32]

$$S_i = \frac{V(y) - V(E(y|\mathbf{x}_{-i}))}{V(y)} \tag{6}$$

The total variance associated with the model is indicated with $V(y)$. The conditional variance term $V(E(y|\mathbf{x}_{-i}))$ indicates the variance of the model determined by excluding the ith term. A more extensive discussion on sensitivity indices computed with the approach described in Eq. (6) can be found elsewhere [10,11].

The sensitivity index S_i provides a quantitative measure of the contribution of the ith term to the variance of the performance y. The sensitivity indices are computed for all the terms of the model indicated in Eq. (2) and shown to the design team in the form of bar plots (see also Sec. IV).

The information on the contribution of each design variable, and every (interaction or higher-order) term involving it, to the output variance provides insight on which variables to focus to improve the performance. At the same time it tells which parameters to carefully modify in subsequent phases of the design process to avoid large deviations from the original baseline design. Contour plots and response surfaces can be presented to the design team only considering the most relevant factors from the sensitivity analysis, thus limiting the information presented but still capturing the most important phenomena. Contour plots allow for a fast and effective analysis of boundaries and constraints, as will be shown in Sec. V. The complete algorithm for PROA is schematically summarized in Fig. 3.

One possible drawback of using a second-order model like the one described by Eq. (2) is that it would not represent a reasonable approximation in the presence of higher-order effects. This would result in a lack-of-fit of the regressor and/or in a low value of the coefficient of determination [33]. The presence of lack-of-fit would also influence the sensitivity indices that describe the contribution of the terms of the model to the regression sum-of-squares only,

neglecting the error sum-of-squares. This phenomenon can be mitigated by, for instance, adding sample points within the CCD to fit higher-order regression models until lack-of-fit is reduced to acceptable levels [33,34]. However, for relatively small regions spanned by the CCD, the results obtained using the model in Eq. (2) can be sufficiently accurate to account for all (or most of) the variability of the output of the simulations [34].

One last remark regards the computational cost required by PROA. The required number of simulations for the full-factorial part of the CCD increases proportionally with the number of design variables. Methods exist to reduce this computational cost, still providing a structured (and balanced) design, considering continuous and discrete design variables. We refer to the possibility of creating Resolution V, Resolution IV, and Resolution III factorial designs [33–36]. The Pareto-robustness metric is independent from the number of simulations performed in the proximity of each optimal solution. Its meaning, instead, together with the meaning and validity of the response surfaces and the validity of the regression-based sensitivity analysis, is instead dependent on the number of sample points used in the analysis. The designer shall be careful in selecting a factorial design that provides a number of sample points at least equal to the number of regression coefficients to estimate, plus one. For a more complete discussion on regression analysis the reader is referred to the textbooks of Kuri and Cornell [36] and Draper and Smith [33].

The results of the validation of PROA are provided in the Appendix. In the next section, PROA is implemented for the design of a satellite for Earth observation instead. The main purpose is to show the possibility of driving the engineering team and the decision-makers toward a specific region of PF_{known} using PROA, and to allow for a more detailed local analysis exploiting the CCD-generated solutions.

III. Case Study: Earth-Observation Mission

On 26 December 2004, the earthquake of Sumatra–Andaman, the largest seismic event in forty years, produced a devastating tsunami that affected the region of the Indian Ocean called the Bay of Bengal and the Indonesian region [37]. To illustrate the methodology described in the previous section we consider an Earth-observation mission with the following mission statement as driver for the design: "Design an Earth-observation mission to provide disaster management tools for the Bay of Bengal and Indonesian regions, for over a period of 7 years."

From the mission statement, we find that the mission should be focused on the observation of a well-determined area on the globe, delimited by latitudes 12 deg S and 20 deg N, and longitudes 75 and 120 deg E. Further, top-level requirements for a satellite mission in support of response and postdisaster operations are related to spatial resolution, coverage, and revisit time [38].

Two classes of spatial resolution are considered strategic: 3 and 30 m spatial resolution images both obtainable with synthetic aperture radars and optical payloads [38,39], of which we will choose the latter. The objective of the analysis is now defined as to obtain the largest total target-area coverage (considering a fixed simulation time period for each design vector, i.e., three days), with the best possible image spatial resolution, and at minimum cost. The objectives and constraints considered for the analysis are summarized in Table 1. The ratio between the total coverage and the number of simulation days allows for estimating the average target-area coverage per day, and as a consequence providing a measure proportional to the average revisit time of the satellite over the entire target area.

The mathematical models of a satellite, with its main subsystems have all been designed and implemented. The main relationships between the design parameters have been derived from the subsystems' mathematical models available in [40–42]. As shown in [43], these models have been verified and validated. Some of the main design variables needed for the sizing of the aforementioned subsystems have been considered in the analysis, as shown in Table 2. In Table 3, the related architectural variables and the levels they can assume are presented.

The orbit and coverage models have been adapted from [42–44] and coupled with the subsystems' models. The orbit of the satellite includes the effects due to the main environmental conditions, e.g., atmospheric drag, eclipse conditions, coverage, and target view geometry. The maneuvers that the satellite shall perform are computed as a function of the boundary conditions coming from the launcher-selection process, the inherent satellite properties and the selected orbital parameters.

Once the orbit has been selected and the mission characteristic velocity computed, for a given launcher the payload capability for the selected orbit can be determined using data from [40] and [44].

The launcher characteristic velocity is defined as the total velocity that can be delivered for a given payload after a due east launch from Cape Canaveral and the use of a 185 km parking orbit. We assume that the mission and launcher characteristic velocities are equivalent. The data flow between launcher, satellite, ground segment, and mission models is shown in Fig. 4.

The cost of the mission, which is one of the objectives to be minimized, is computed summing up the launch cost, and the cost of the satellite system and operations. The cost estimating relationships (CERs) have been derived from [40,41]. A hybrid cost model considering the unmanned spacecraft cost model and the small satellites cost model has been implemented. Most of the CERs are related to the mass of the subsystems, the technology readiness level (TRL) the power consumption and the particular technology in use (e.g., three-axis attitude-control technology has a larger cost coefficient than spinned attitude-control technology).

The spatial resolution of the optical payload is linked to its physical dimensions and to the orbit by the following relationship [40]:

$$X_{\text{nadir}} = 2.44 \cdot \frac{h\lambda}{D} \tag{7}$$

where X_{nadir} is the ground diffraction limited spatial resolution at the satellite nadir expressed in m, h is the altitude of the satellite above the nadir point expressed in m, λ is the wavelength of the radiation that we want to observe ($\approx$0.5 μm in the case of visible light). The variable D represents the aperture diameter of the optical instrument expressed in m. From Eq. (7) it can be concluded that the ground spatial resolution at nadir is higher (lower value of X_{nadir}) than the spatial resolution at the end of the swath width, because the distance from the satellite to the edge of the swath is larger. To compute the spatial resolution on the target area an average resolution has been taken into account for each satellite passage over the target area itself.

This is a typical preliminary-design example at an early development stage, which fits the purpose of presenting the potentialities of PROA.

IV. Results and Discussions

In Fig. 5 the Pareto front obtained after the global optimization phase is shown. The NSGAII has been executed with a population size of 250 individuals for 150 generations. The results of the simulations show that PF_{known} presented in Fig. 5 does not significantly change already after the 120th generation.

As can be observed from Fig. 5, the spatial resolution and the coverage show a contrasting behavior and a nonconvex local Pareto front (see the projections for the combinations of the two variables). This means that solutions with a large coverage also exhibit a worse performance in terms of average spatial resolution on the target area. Also the mission cost and the spatial resolution present a conflicting behavior.

A local analysis on PF_{known} shows that indeed not all solutions in Fig. 5 are equally Pareto-robust, and for some of them unfeasible designs were generated after dispersing the design variables. This local improvement phase for PF_{known} provides the ranking of the solutions according to their Pareto-robustness. In Fig. 6, projections of PF_{known} on the three planes with the most Pareto-robust solution are shown; thicker triangles and crosses represent clusters of solutions close to each other in the objective space.

We also searched for the least Pareto-robust solution (not shown here): it presents a much worse constraint-violation behavior if compared with the most Pareto-robust one. Indeed, considering the 273 design vectors generated with the CCD, the most Pareto-robust solution presents 129 feasible and 144 infeasible solutions with all the violations only determined by the spatial resolution constraint. The least Pareto-robust solution only presents 4 feasible solutions. The remaining 269 are all infeasible with violations of all the constraints. Amongst the design vectors generated by the local analysis, 6 of them improve PF_{known}, dominating 13 original solutions.

The local analysis already eliminates many options to be evaluated by the design team providing the most Pareto-robust solution amongst the optimal solutions. Thus, the design team already has a much more clear idea on probably the most interesting region of the design space in which to focus the attention, the discussions, and the tradeoffs. Further insight can be gathered through the global sensitivity analysis and the regression analysis for the design region of interest. In Table 4 the design-variable settings of the most Pareto-robust solution are presented. The simulations have shown that the solutions on PF_{known} all have converged toward a value of nine for the TRL, three for the type of solar cells, and two for the type of battery design variables. The TRL has an influence on the cost of the mission; thus, a logical conclusion is that the optimizer converges toward the maximum value, i.e., the value that minimizes the cost. The solar cells with intermediate efficiency, intermediate power density, and intermediate cost are considered to be the best compromise. The same balance has been obtained in case of the battery selection, see Table 3. Not much influence of these three variables in the determination of the objectives has been detected, thus, to simplify the discussion of the results obtained with ANOVA and regression analysis, from this point onward they are considered to be frozen to the values obtained from the optimization phase. In Table 4, the design-variable settings used for the CCD analysis are also presented. The central point of the CCD does not coincide with the original optimal design vector, because the CCD center was shifted to avoid constraint violation in the design space. The solution identified as the most Pareto-robust one presents a satellite in a nonsun-synchronous medium Earth orbit. These unusual settings for an Earth-observation mission come from the inherent assumptions made on the model, e.g., the effect of the radiation environment is not taken into account, and one single satellite is allowed to take part in the scenario. However, this is also due to the fact that the optimization has been left free from many constraints concerning the ranges of the design variables, e.g., the semimajor axis, leading to a condition for which the swath-width is large, and the inclination allows for an almost constant coverage of the target area.

In Table 4, Launcher 8 represents an AtlasD/Centaur (two-stage), Launcher 9 represents an AtlasD/Centaur/TE364-4 (three-stage), and Launcher 10 represents a TitanIIIC Centaur (three-stage) [40,44].

In Figs. 7 and 8 the results obtained with the ANOVA and variance decomposition on the most Pareto-robust region of the design space are presented. The bars represent the percentage contribution of the factors (see Table 4 for nomenclature), their interactions (when the product of two factors is indicated), and their quadratic effects (when the product of the factor by itself is indicated) to the variability of the constraints and the objectives. These bars have been computed using Eq. (6) for all the terms of Eq. (2). In the design region spanned by the CCD very small lack-of-fit was detected (i.e., 0.5%), meaning that the quadratic model described by Eq. (2) was sufficient to effectively fit the data and to properly explain the variability of the performance.

The simulations demonstrated that in this region of the design space the *on-orbit-mass* and the *perigee-altitude* constraints are never violated. Thus, the bar plots of Fig. 7 indicate the variables that contribute the most to getting close to the relative constraints.

In Fig. 7, it can be observed that the launcher selection (H) is the factor that mostly affects the on-orbit-mass constraint. There is also a small quadratic effect, due to the fact that launchers 8 and 10 (the minimum and maximum value in the CCD, because launcher 9 is the central point) have a lower payload capability for characteristic velocities that are larger than 11.8 km/s. The semimajor axis (B) and inclination (C) of the final orbit also play an important role in this region of the design space. Indeed, together they determine the mission-characteristic velocity. With increasing mission-characteristic velocity the available payload on orbit decreases. The payload-aperture diameter and the other factors affect this constraint mostly as a quadratic effect, indicating that the minimum constraint violation is probably somewhere in the middle of the design region spanned by the CCD. In Fig. 7b, it can be observed that the perigee-altitude constraint is mostly affected by the semimajor axis (B) and to a far lesser extent the eccentricity (A) of the selected orbit.

The *spatial resolution* constraint (Fig. 7c) is practically only affected by the semimajor axis (B) and the payload-aperture diameter (D), with a small interaction between them. With increasing altitude the spatial resolution of the instrument gets lower, while with an increasing optical-payload aperture diameter the spatial resolution tends to improve. The downlink-margin constraint is mainly affected by the semimajor axis (B), the transmitter RF output power (E), and the antenna aperture diameter (F), see Fig. 7d. The downlink-margin is related to the distance at which the communication with the ground station takes place, the power with which the signal is emitted and the directionality of the antenna, linked to its aperture for a parabolic reflector type.

The cost of the mission is computed as the sum of spacecraft and launcher cost. The spacecraft cost is determined from the CERs mentioned in the previous section, mostly as a function of the mass of the spacecraft, which in turn is affected by the payload mass and thus by the aperture diameter (D) the most, as shown in Fig. 8a.

The coverage of the target area is determined by the eccentricity (A), the semimajor axis (B), and the inclination (C) of the orbit, Fig. 8b. The prominent interaction between the semimajor axis and the inclination is due to the combined effect of these two design variables. For instance, a large value for the semimajor axis would in principle increase the coverage, even though it would worsen the spatial resolution performance (see Fig. 8c). However, the extent to which the coverage increases depends on the inclination of the orbit. If there is no intersection between the satellite ground-track and the target area, then increasing the semimajor axis to increase the coverage would provide a less effective result compared with the case in which the ground track passes through the target area. As already anticipated, the spatial resolution depends almost entirely on the semimajor axis (B), but reasonably also on the aperture-diameter of the payload instrument (D), although in the current analysis this is only a small effect.

With this acquired knowledge about the most relevant factors in the design region of interest, the actual relationships between the design variables and objectives and constraints can be computed and shown to the design team in the form of contour plots.

In some of the graphs shown from Figs. 9–13 contour plots involving architectural (i.e., discrete) variables are shown. They have no physical relevance, because only few of the points on the contour are valid. However, they are very useful to understand the trends of the performances and to provide visual information to the design team. In these figures some black dots are also shown. They represent a hypothetical design baseline that can be derived from the combined analysis performed with the variance decomposition and the contour plots in the most Pareto-robust region of the design space. The rationale behind this baseline is discussed in the subsequent paragraphs.

In Fig. 9 the trend of the mission cost as a function of the payload aperture diameter and the launcher selection is shown. The cost increases for increasing payload-aperture diameter and with the launcher selection going from 8 to 10. The analysis we performed shows that in this region of the design space, if one would modify the semimajor axis from low to intermediate level, the cost figure would not change, but the spatial resolution constraint would be violated in the entire region (no feasible solutions in this region).

The variance decomposition in Fig. 7 shows that the launcher selection only affects the on-orbit-mass constraint, but it has already been pointed out that in the design region spanned by the CCD defined in Table 4 this constraint is never violated. This means that by selecting launcher 8 instead of 9, there is a cost savings without affecting the performance and the constraints. To illustrate this, the graphs in Figs. 10–13 have been obtained using launcher number 8.

The target-area *coverage* objective is mainly affected by the orbital parameters considered in the simulation, i.e., eccentricity, inclination, and semimajor axis, see Fig. 8b. In Fig. 10, the target-area coverage is plotted against the semimajor axis and the inclination. The infeasibility is determined by the violation of the *spatial-resolution* constraint for increasing semimajor axis. The difference between Figs. 10 and 11 is the value of the eccentricity, which is larger in Fig. 11. The target-area coverage is maximized for a low value of eccentricity. This is due to the fact that the balance between the coverage at apogee and perigee of an eccentric orbit, with the eccentricity within the range determined by the CCD of Table 4, gives a worse performance than an almost circular orbit. The target-area coverage increases with increasing semimajor axis and the inclination getting close to an intermediate value.

The average spatial resolution on the target area is mainly determined by the semimajor axis and the payload aperture-diameter, as shown in Fig. 8c. In Fig. 12 the trends of the spatial-resolution objectives are presented. As can be observed, it gets worse with decreasing payload aperture-diameter, but most prominently it gets worse with increasing semimajor axis. In this case the constraint violation is more clear, because it is drawn in the same space as the objective.

In Fig. 13, the *downlink-margin* is plotted against the transmitter RF power-output and the transmit-antenna diameter. The graph is presented to show that this constraint is violated only for a large telemetry data rate, in combination with a nominal, or higher, value of the semimajor axis, a low transmitter output power, and a low antenna diameter.

The combination of launcher 8 and a low payload aperture-diameter minimizes the cost and allows for meeting the spatial-resolution constraint if the semimajor axis is in the lowest interval defined by the CCD (Table 4). This combination of design variables, together with an intermediate inclination of the orbit around 20 deg, also provides a good balance with the coverage of the target area. The downlink-margin constraint is not violated if the semimajor axis is in the lowest part of the interval and the telemetry data rate is at its nominal level, even with a low RF transmitter-power output and low satellite-antenna aperture diameter. These two design variables do not contribute much to the determination of the other objectives and constraints, thus leaving the design team with a certain freedom of selecting their levels.

The selected design point, i.e., the black dot, is presented in Table 5. It provides a solution that is still on the Pareto front and does not violate the constraints. The solution has been defined preferring the cost and the coverage over the spatial resolution. Many other design points could have been selected, but the fundamental aspect is that the selection took place in a Pareto-robust design region, with a clear insight in the effect of the variables on objectives and constraints, and with a clear picture of the shape of the design space with the variation of objectives and constraints.

The PROA as presented in this paper was used to study the effect of the modification of the design variables on the objectives in terms of robustness with respect to the Pareto front. Considering uncontrollable factors in the analysis of the Pareto-optimal solutions, instead, would lead to a type of analysis with a modus operandi much closer to reliability engineering. In this case, the Pareto-robustness metric could still be implemented to provide an indication of the variability (in the Pareto sense) of all the objectives due to the uncertain behavior of uncontrollable factors.

V. Conclusions

In this paper, a methodology for the postoptimality study of complex systems has been presented. It has been named the Pareto-robust optimization approach (PROA). Previous studies demonstrated that not all the mathematically optimal solutions are also optimal from an engineering point of view. Robustness should also be taken into account.

The results discussed in this paper demonstrate that PROA is able to compute the Pareto-robustness of the mathematically optimal solutions, correctly steering the attention of the design team on the most Pareto-robust regions of the design space. Further, PROA is able to improve the known Pareto front, pushing it toward the true Pareto front of the test cases proposed, and to graphically support the major tradeoffs for the decision-making process. The Pareto-robustness metric introduced in this paper is independent from the specific method used to compute the Pareto front, because it is solely based on the Pareto-dominance principle, and it is applied after the computation of the Pareto front itself.

The analysis of the test case of an Earth-observation mission shows that the combination of a global multi-objective optimization method with PROA effectively drives the design process, limiting the effort of the engineering team in the search for a single optimal and robust (Pareto-robust) design region. Indeed, the design region selected by PROA provides solutions that are far from three of the constraints, while still remaining close to the initially known Pareto front. The graphical information on quantitative sensitivity analysis presented in the form of bar plots and contour plots with the constraints can be considered a valuable aid for the engineering team, providing much more insight in the problem than any other single-point design methodology. A detailed analysis of the contour plots allows for the selection of a baseline design by balancing the objectives and constraints in a very effective graphical fashion.

Appendix A: Validation Examples

In this section, two validation examples are presented to demonstrate the performance of the PROA to identify robust and nonrobust solutions on $\mathrm{PF}_{\mathrm{known}}$.

The first example is an unconstrained multi-objective problem initially proposed by Deb [45] and modified by Tan et al. [21], of which we consider a further modification. The problem statement is

$$\text{Minimize } \mathbf{f}(\mathbf{x}) = \left[x_1, \frac{1}{x_1}\prod_{j=1}^{3} g_j\right] \quad \text{where } 0.1 \le x_1 \le 1.5 \quad \text{and}$$

$$0 \le x_j \le 1.5$$

$$g_j = 2.02 - \exp\left\{-\left(\frac{x_j - 0.1}{0.015}\right)^2\right\} - 1.0175 \cdot \exp\left\{-\left(\frac{x_j - 0.9}{0.4}\right)^2\right\}$$

$$\forall\ j = 2,3,4 \tag{A1}$$

For the second test problem, three constraints have been added to the previous one:

$$g_j < -\exp\{(x_j - 0.2)^3\} + 4 \quad \forall\ j = 2,3,4 \tag{A2}$$

The PF presented in Fig. A1 is obtained with NSGAII, using a population size of 40 with 200 generations. Using PROA an analysis is performed on PF_{known} and the results are presented in Figs. A1b and A1c. For each Pareto-optimum point, the design variables are dispersed with 5% of their interval, according to the CCD structure, obtaining the design vectors represented by the black squares. Finally, the most Pareto-robust and least Pareto-robust solutions are determined. The triangles and the diamonds represent the objective-vectors obtained from all the design vectors determined by the CCD in correspondence of these most and least Pareto-robust solutions, respectively. The most Pareto-robust solution is obtained with $x_1 = 1.5$ and $x_{2,3,4} = 0.9$. The least Pareto-robust solution is obtained with $x_1 = 0.1$ and $x_{2,3,4} = 0.1$, instead. This is an expected result due to the structure of the problem. Indeed, in Fig. A2b, neglecting the constraint for now, the shape of the function g_j confirms that the optimal solutions are obtained with $x_{2,3,4} = 0.1$ or equivalently $x_{2,3,4} = 0.9$, but the minimum obtained with $x_{2,3,4} = 0.1$ is much steeper (thus less robust) if compared with the minimum in correspondence of $x_{2,3,4} = 0.9$. Further, the modification of x_1 when it is closer to its upper bound causes the CCD-generated vectors to be closer to the PF if compared with the case when x_1 is closer to its lower bound. The black circles in Fig. A1 (see the zoom-in of Fig. A1c) show that PROA, during its search for Pareto-robust solutions, is also capable of providing additional Pareto-optimal solutions.

The three constraints added for the second test problem causes the results to be completely overturned. As shown in Fig. A2b, the exponential function(s) intersects the g_j function(s) very close to 0.9, which is the location for which the most Pareto-robust solution was found in the unconstrained case. Indeed, for the second test problem, the least Pareto-robust solution is obtained with $x_1 = 0.1$ and $x_{2,3,4} = 0.9$. These variable settings cause many of the CCD-generated design vectors to violate the constraints, as represented by the cross symbols in Fig. A2. The most Pareto-robust solution, in this case, is represented by the steep peak ($x_1 = 1.5$ and $x_{2,3,4} = 0.1$), because it is the one that causes no constraint violations, amongst the Pareto-optimal solutions, with the CCD-generated vectors closer to the PF (because x_1 is at its upper bound).

References

[1] Pardalos, P. M., and Romeijn, H. E., *Handbook on Global Optimization*, Vol. 1/2, Kluwer Academic Publishers, Norwell, MA, 2002.

[2] Back, T., Fogel, D. B., and Michalewicz, Z., *Handbook of Evolutionary Computation 1-2*, Inst. of Physics Publishing, Bristol, 1997.

[3] Goldberg, D. E., *Genetic Algorithms in Search, Optimization and Machine Learning*, Addison Wesley Longman, Reading, MA, 1989.

[4] Kennedy, J., Eberhart, R. C., and Shi, Y., *Swarm Intelligence*, Morgan Kaufman, San Mateo, CA, 2001.

[5] Shukla, P. K., and Deb, K., "On Finding Multiple Pareto-Optimal Solutions Using Classical and Evolutionary Generating Methods," *European Journal of Operational Research*, Vol. 181, No. 3, 2007, pp. 1630–1652.
doi:10.1016/j.ejor.2006.08.002

[6] Deb, K., *Multi-Objective Optimization Using Evolutionary Algorithms*, Wiley, New York, 2001.

[7] Coello, C. A., Lamont, G. B, and Van Veldhuizen, D. A., *Evolutionary Algorithms for Solving Multi-Objective Problems*, Genetic and Evolutionary Computation Series, Springer, New York, 2007.

[8] Nakamura, M., Izui, K., Nishiwaki, S., and Yoshimura, M., "A Multi-Objective Particle Swarm Optimization Incorporating Design Sensitivities," *11th AIAA/ISSMO Multidisciplinary Analysis and Optimization Conference*, AIAA Paper 2006-6910, 2006.

[9] Izui, K., Nishiwaki, S., and Yoshimura, M., "Swarm Algorithms for Single- and Multi-Objective Optimization Problems Incorporating Sensitivity Analysis," *Engineering Optimization*, Vol. 39, No. 8, 2005, pp. 981–998.
doi:10.1080/03052150701552774

[10] Ridolfi, G., Mooij, E., and Corpino, S., "Complex-Systems Design Methodology for Systems-Engineering Collaborative Environment," *Systems Engineering–Practice and Theory*, edited by Cogan, B., InTech, March 2012.

[11] Ridolfi, G., Mooij, E., Cardile, D., Corpino, S., and Ferrari, G., "A Methodology for System-of-Systems Design in Support of the Engineering Team," *Acta Astronautica*, Vol. 73, April–May 2012, pp. 88–99.
doi:10.1016/j.actaastro.2011.11.016

[12] Mitten, L. G., "Branch-and-Bound Methods: General Formulation and Properties," *Operations Research*, Vol. 18, No. 1, 1970, pp. 24–34.
doi:10.1287/opre.18.1.24

[13] Alefeld, G., and Mayer, G., "Interval Analysis: Theory and Applications," *Journal of Computational and Applied Mathematics*, Vol. 121, Nos. 1–2, 2000, pp. 421–464.
doi:10.1016/S0377-0427(00)00342-3

[14] Abo–Sinna, M. A., and Hussein, M. L., "An Algorithm For Generating Efficient Solutions of Multi-Objective Dynamic Programming Problems," *European Journal of Operational Research*, Vol. 80, No. 1, 1995, pp. 156–165.
doi:10.1016/0377-2217(93)E0219-N

[15] Bellman, R. E., and Dreyfus, S. E., *Applied Dynamic Programming*, Princeton Univ. Press, Princeton, NJ, 1962.

[16] Das, I., and Dennis, J. A., "Normal-Boundary Intersection: A New Method for Generating the Pareto Surface in Nonlinear Multicriteria Optimization Problems," *SIAM Journal of Optimization*, Vol. 8, No. 3, 1998, pp. 631–657.
doi:10.1137/S1052623496307510

[17] Kim, I. Y., and de Weck, O. L., "Adaptive Weighted Sum Method for Bi-Objective Optimization," *Structural and Multidisciplinary Optimization*, Vol. 29, No. 2, 2005, pp. 149–158.
doi:10.1007/s00158-004-0465-1

[18] Erfani, T., and Utyuzhnikov, S. V., "Direct Search Domain: A Method for Even Generation of Pareto Frontier in Multi-Objective Optimization," *Engineering Optimization*, Vol. 43, No. 5, 2010, pp. 1–18.
doi:10.1080/0305215X.2010.497185

[19] Messac, A., and Mattson, C. A., "Normal Constraint Method with Guarantee of Even Representation of Complete Pareto Frontier," *AIAA Journal*, Vol. 42, No. 10, 2004, pp. 2101–2111.
doi:10.2514/1.8977

[20] Sanguthevar, R., "On Simulated Annealing and Nested Annealing," *Journal of Global Optimization* Vol. 16, No. 1, 2010, pp. 43–56.
doi:10.1023/A:1008307523936

[21] Tan, K. C., Khor, E. F., Lee, T. H., and Yang, Y. J., "A Tabu-Based Exploratory Evolutionary Algorithm for Multi-Objective Optimization," *Artifcial Intelligence Review*, Vol. 19, No. 3, 2003, pp. 231–260. doi:10.1023/A:1022863019997

[22] Glover, F., "Tabu Search Part I/II," *ORSA Journal on Computing*, Vols. 1–2, 1990, pp. 4–32, 190–206.

[23] Coello, C. A. C., Pulido, T. G., and Lechuga, S. M., "Handling Multiple Objectives with Particle Swarm Optimization," *IEEE Transactions on Evolutionary Computation*, Vol. 8, No. 3, 2004, pp. 256–279. doi:10.1109/TEVC.2004.826067

[24] Fonseca, C. M., and Fleming, P. J., "An Overview of Evolutionary Algorithms in Multi-Objective Optimization," *Evolutionary Computation*, Vol. 3, No. 1, 1995, pp. 1–16. doi:10.1162/evco.1995.3.1.1

[25] de Weck, O. L., Miller, D. W., and Mosier, G. E., "Multivariable Isoperformance Methodology for Precision Opto-Mechanical Systems," AIAA Paper 2002-1420, 2002.

[26] Messac, A., and Mattson, C. A., "Generating Well-Distributed Sets of Pareto Points for Engineering Design Using Physical Programming," *Optimization and Engineering*, Vol. 3, No. 4, 2002, pp. 431–450. doi:10.1023/A:1021179727569

[27] Deb, K., Pratap, A., Agarwal, S., and Meyarivan, T., "A Fast and Elitist Multi-Objective Genetic Algorithm: NSGA-II," *IEEE Transactions on Evolutionary Computation*, Vol. 6, No. 2, 2002, pp. 182–197. doi:10.1109/4235.996017

[28] Zitzler, E., Deb, K., and Thiele, L., "Comparison of Multi-Objective Evolutionary Algorithms: Empirical Results", *Evolutionary Computation*, Vol. 8, No. 2, 2000, pp. 173–195. doi:10.1162/106365600568202

[29] Deb, K., Thiele, L., Laumanns, M., and Zitzler, E., "Scalable Test Problems for Evolutionary Multi-Objective Optimization," edited by Abraham, A., Jain, L. C., and Goldberg, R., *Evolutionary Multi-Objective Optimization: Theoretical Advances and Applications*, Springer, New York, 2005, pp. 105–145.

[30] Deb, K., Gupta, S., Daum, D., and Branke, J., "Reliability-Based Optimization Using Evolutionary Algorithms," *IEEE Transactions on Evolutionary Computation*, Vol. 13, No. 5, 2009, pp. 1054–1074. doi:10.1109/TEVC.2009.2014361

[31] Jin, Y., and Branke, J., "Evolutionary Optimization in Uncertain Environments: A Survey," *IEEE Transactions on Evolutionary Computation*, Vol. 9, No. 3, 2005, pp. 307–317. doi:10.1109/TEVC.2005.846356

[32] Saltelli, A., Tarantola, S., Campolongo, F., and Ratto, M., *Sensitivity Analysis in Practice. A Guide to Assessing Scientific Models*, Wiley, New York, 2004.

[33] Draper, N. D., and Smith, H., *Applied Regression Analysis*, 3rd ed., Wiley, New York, 1998.

[34] Montgomery, D. C., *Design and Analysis of Experiments*, Wiley, New York, 2001.

[35] Phadke, M. S., *Quality Engineering Using Robust Design*, Prentice-Hall, Englewood Cliffs, NJ, 1989.

[36] Khuri, A. I., and Cornell, J. A., *Response Surfaces. Design and Analysis*, 2nd ed., Marcel Dekker Inc., New York, 1996.

[37] Thorne, L., Hiroo, K., Charles, J. A, Meredith, N., Steven, N. W., Richard, C. A., Susan, L. B., Susan, L. B., Michael, R. B., Rhett, B., Heather, R. D., Göran, E., Kenji, S., and Stuart, S., "The Great Sumatra-Andaman Earthquake of 26 December 2004," *Science*, Vol. 308, No. 1127, 2005, pp. 1127–1133. doi:10.1126/science.1112250

[38] Martimort, P., Arino, O., Berger, M., Biasutti, R., Carnicero, B., Del Bello, U., Fernandez, V., Gascon, F., Greco, B., Silvestrin, P., Spoto, F., and Sy, O., "Sentinel-2: The Optical High-Resolution Mission for GMES Operational Services," ESA Bullettin 131, ESTEC/ESRIN Directorate of Earth Observation Programmes, Aug. 2007, http://www

.esa.int/esapub/bulletin/bulletin131/bul131b_martimort.pdf [retrieved 11 Feb. 2013].

[39] De Bernardinis, B., "GMES Fast Track Emergency Response Core Service," GMES Strategic Implementation Plan, 2007, http://www.czechspace.cz/en/system/files/ERCS_Strategic_Implementation_Plan_Final.pdf [retrieved 11 Feb. 2013].

[40] Wertz, J. R., and Larson, W. J., *Space Mission Analysis and Design*, 3rd ed., Springer, New York, 1999.

[41] Wertz, J. R., and Larson, W. J., *Reducing Space Mission Cost*, Microcosm Press, El Segundo, CA, 2005.

[42] Wertz, J. R., *Mission Geometry: Orbit Constellation Design and Management*, Microcosm Press, El Segundo, CA, 2001.

[43] Ridolfi, G., Mooij, E., and Corpino, S., "A System Engineering Tool for the Design of Satellite Subsystems," AIAA Paper 2009-6037, 2009.

[44] Cornelisse, J. W., Schoyer, H. F. R., and Wakker, K. F., *Rocket Propulsion and Spaceflight Dynamics*, Pitman Publishing, Northern

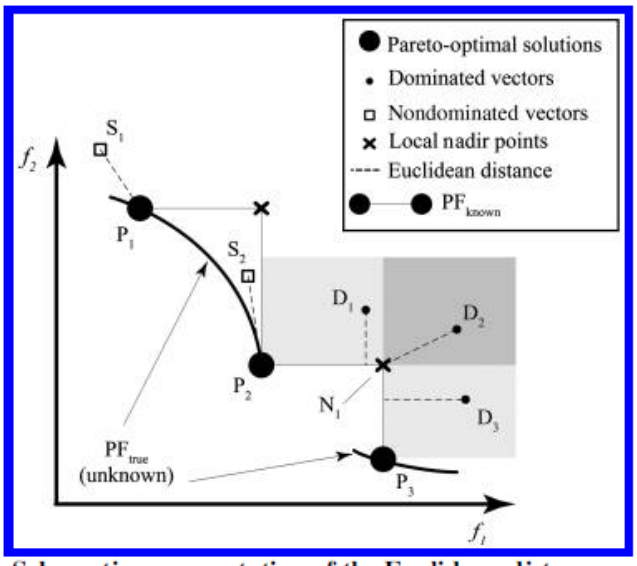

Fig. 1 Schematic representation of the Euclidean-distance operator.

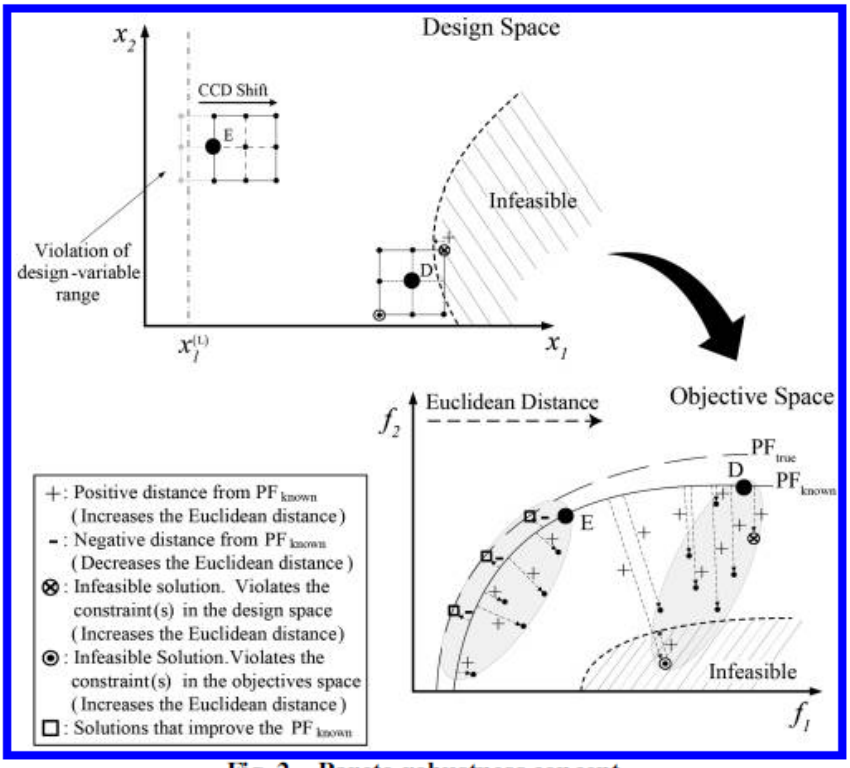

Fig. 2 Pareto robustness concept.

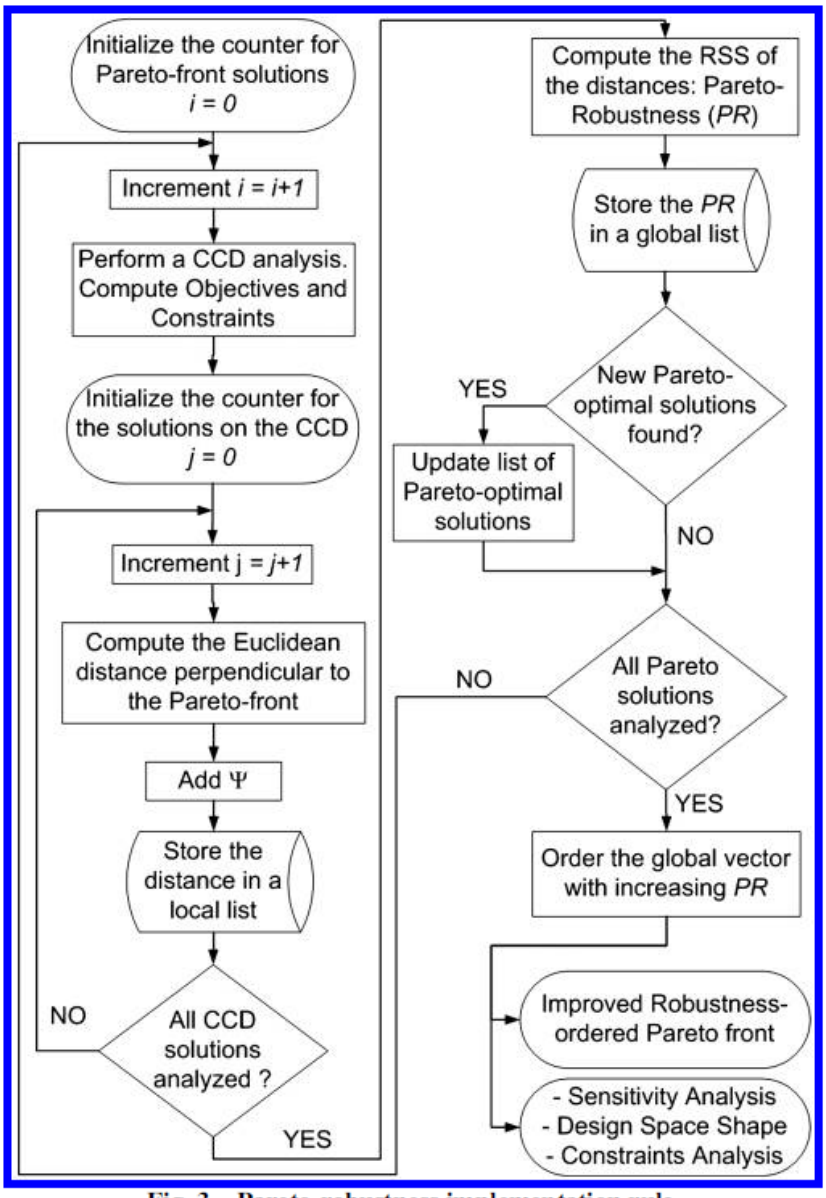

Fig. 3 Pareto-robustness implementation rule.

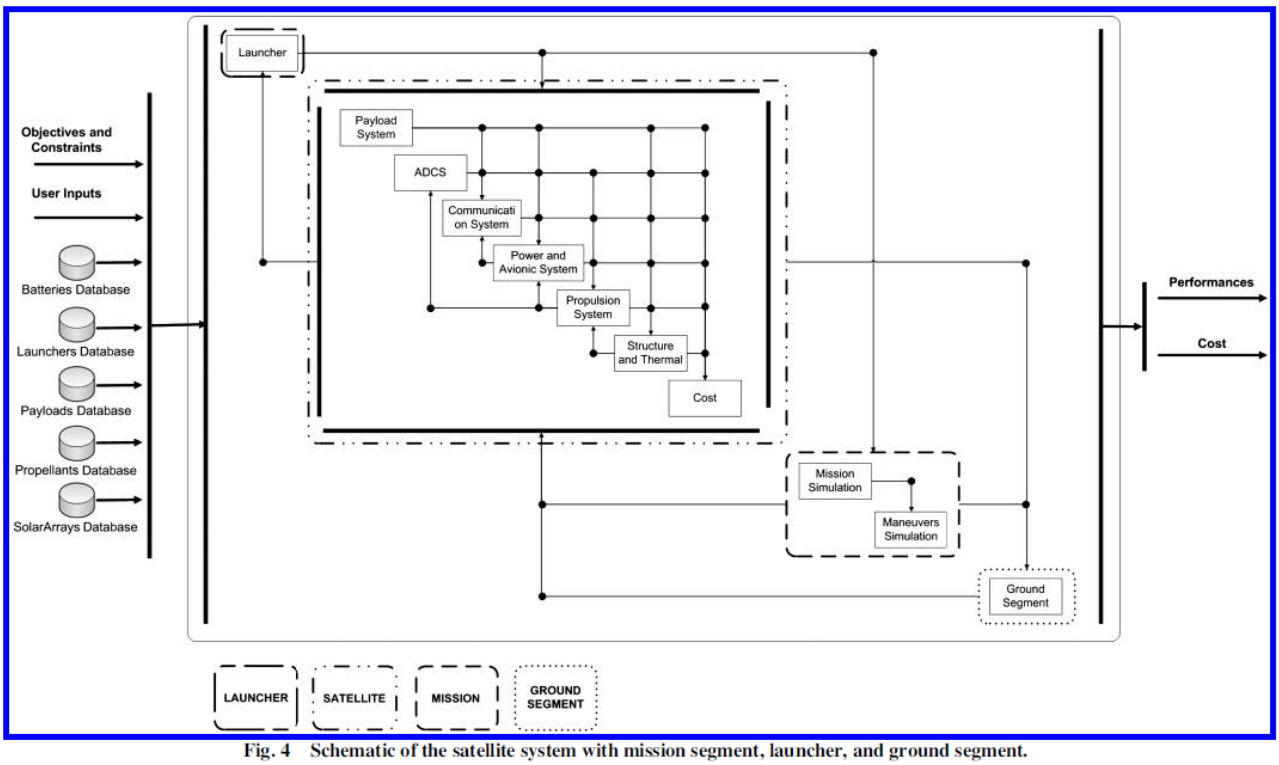

Fig. 4 Schematic of the satellite system with mission segment, launcher, and ground segment.

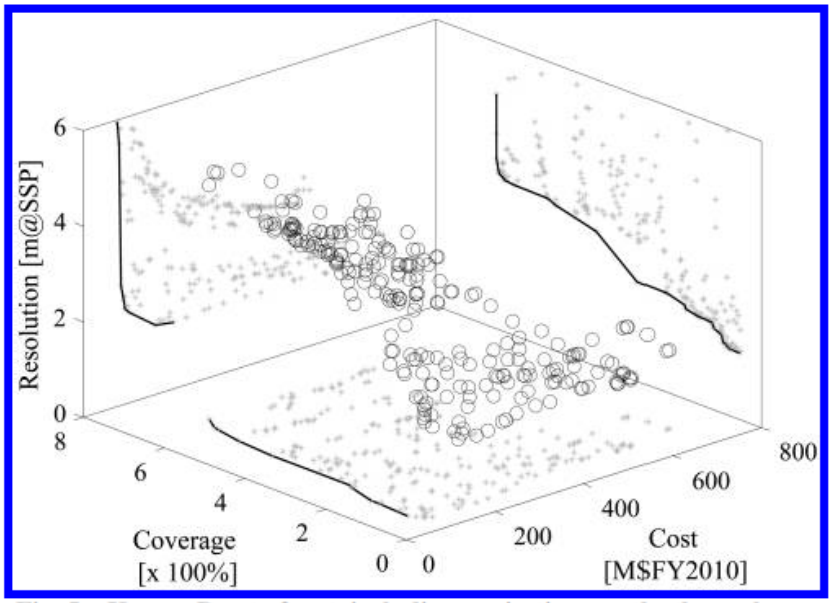

Fig. 5 Known Pareto front, including projections on the three planes.

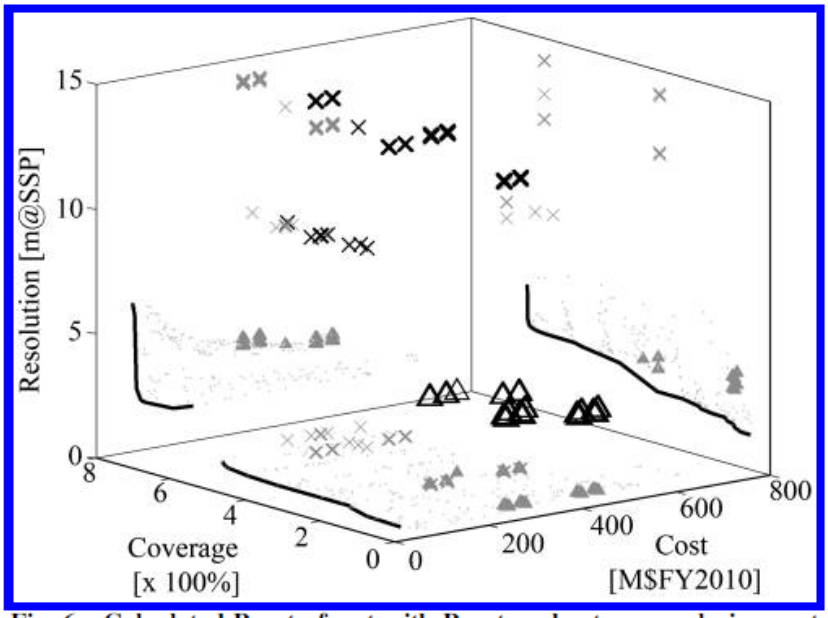

Fig. 6 Calculated Pareto front with Pareto robustness analysis; most Pareto-robust solution. Δ feasible solutions, × infeasible solutions, ▲ projections of the feasible solutions, × projections of the infeasible solutions, and • projections of the solutions on PF_{known}.

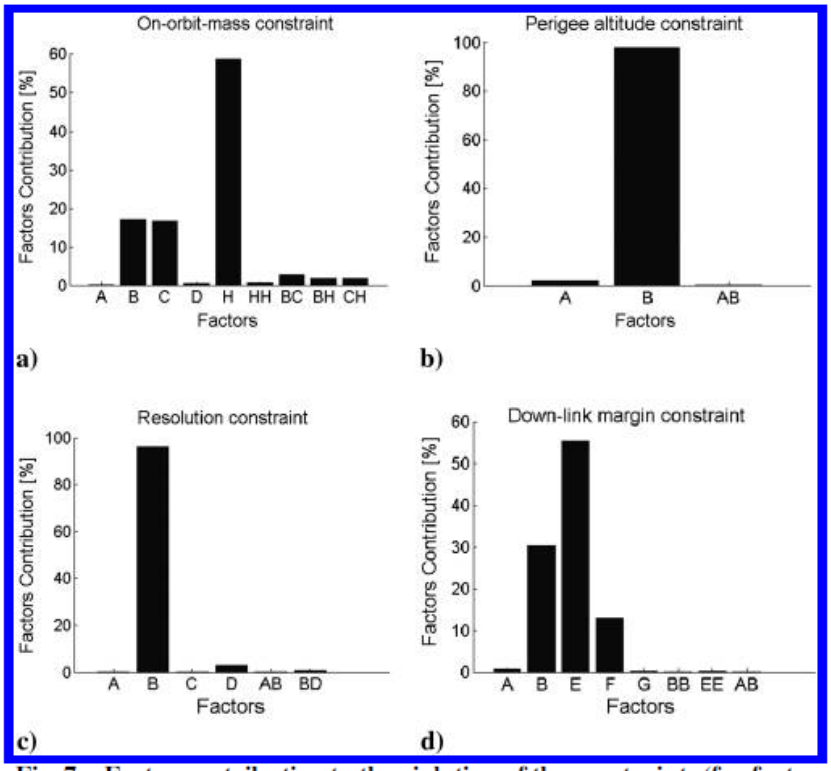

Fig. 7 Factor contribution to the violation of the constraints (for factor notations, see Table 4).

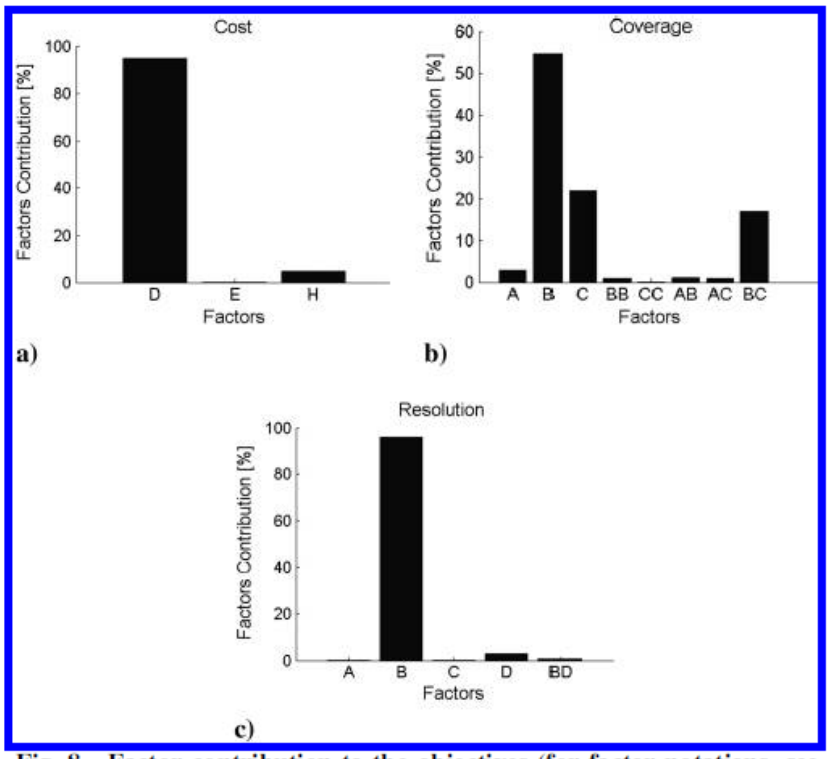

Fig. 8 Factor contribution to the objectives (for factor notations, see Table 4).

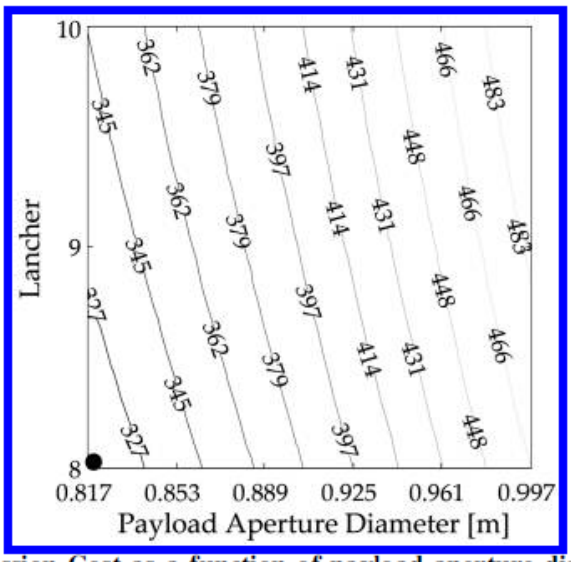

Fig. 9 Mission Cost as a function of payload aperture-diameter and Launcher. The other parameter levels are A_{-1}, B_{-1}, C_0, E_{-1}, F_{-1}, and G_{-1}. The black circle indicates the baseline design.

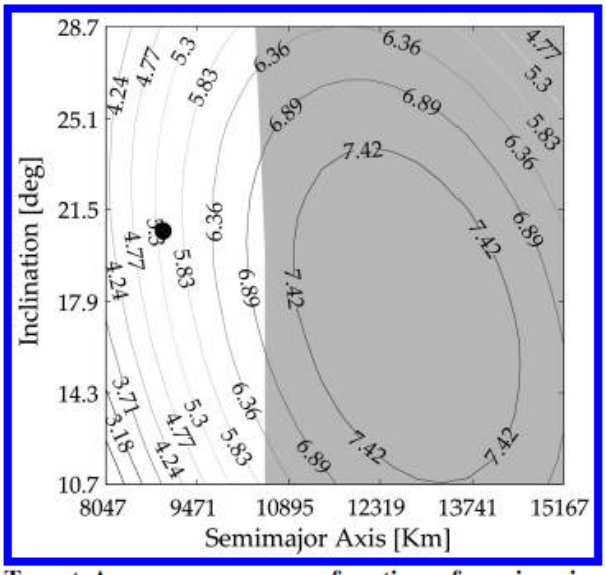

Fig. 10 Target Area coverage as a function of semi-major axis and inclination. Other parameter levels are A_{-1}, D_1, E_{-1}, F_{-1}, G_{-1}, and H_{-1}. Black circle indicates baseline design. Grey area is infeasible.

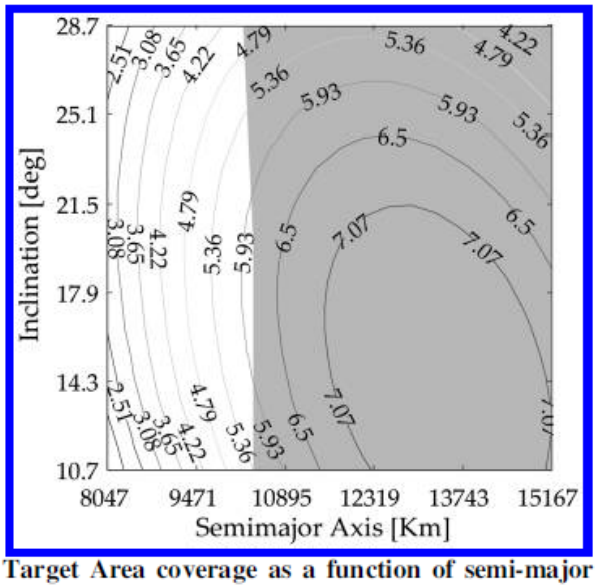

Fig. 11 Target Area coverage as a function of semi-major axis and inclination. Other parameter levels are A_1, D_1, E_{-1}, F_{-1}, G_{-1}, and H_{-1}. Grey area is infeasible.

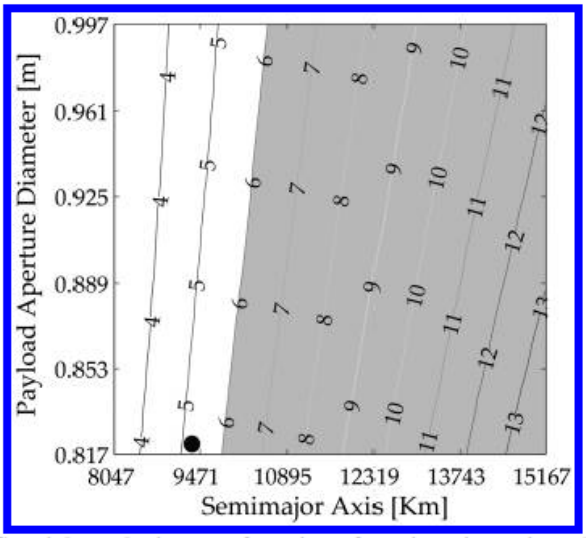

Fig. 12 Spatial resolution as a function of semi-major axis and Payload-aperture diameter. Other parameter levels are $A_{-1}, C_0, E_{-1}, F_{-1}, G_0$, and H_{-1}. Black circle indicates baseline design. Grey area is infeasible.

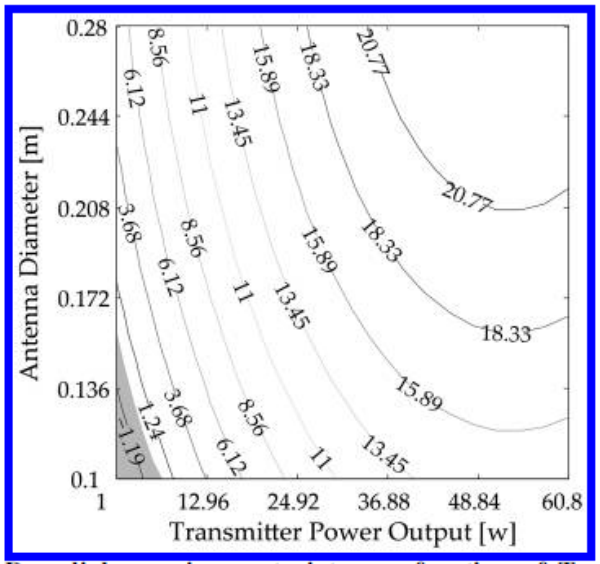

Fig. 13 Downlink-margin constraint as a function of Transmitter-Power output and Antenna diameter. Other parameter levels are A_{-1}, B_0, C_0, D_1, G_1, and H_{-1}. Grey area is infeasible.

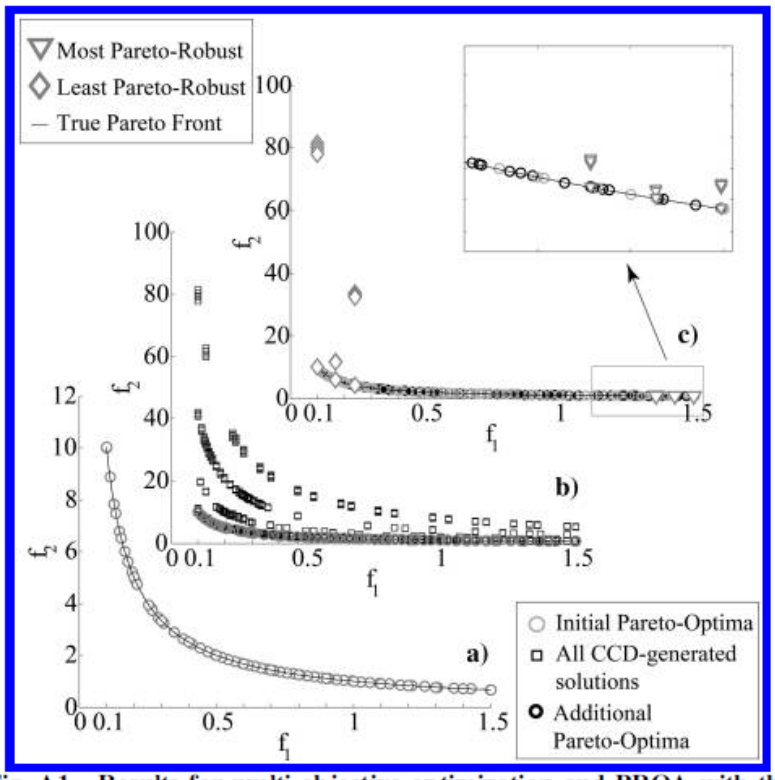

Fig. A1 Results for multi-objective optimization and PROA with the test problem 1.

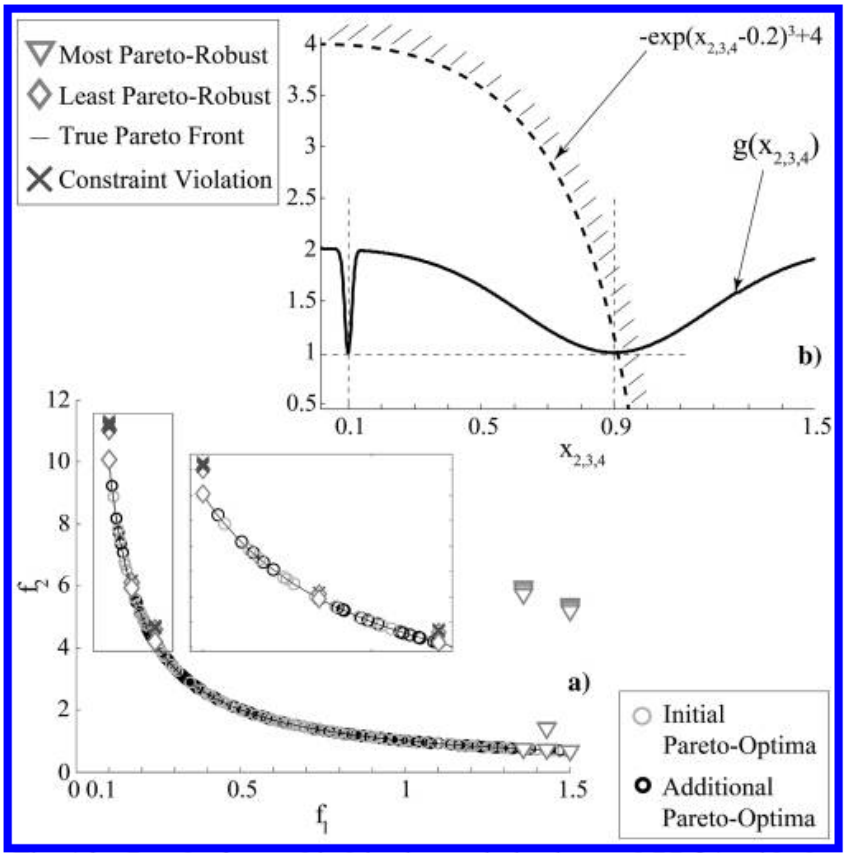

Fig. A2 Results for multi-objective optimization and PROA with the test problem 2.

Table 1 Design objectives and constraints

Objectives
Minimize mission cost [M$FY2010]
Maximize target area coverage [%·100]
Minimize average spatial resolution on the target area [m @ SSP]
Constraints
Satellite mass + adapter mass <= launcher mass availability on orbit
Perigee altitude > 200 Km
Spatialre solution <= 6 m @ SSP
Downlink margin > 4 dB

Table 2 Design factors used in the simulation and relative design intervals

Design Variable	Type	Intervals	
		Min	Max
Eccentricity	Continuous	0	1
Semimajor axis	Continuous	6400, km	42,000, km
Inclination	Continuous	0, deg	180, deg
Payload aperture diameter	Continuous	0.1, m	1, m
Satellite transmitters output power (RF power)	Continuous	1, W	300, W
Satellite aperture-antenna diameter	Continuous	0.1, m	1, m
Telemetry data rate	Continuous	1, Mbps	3, Mbps
Type of solar cells	Architectural	1	3
Type of batteries	Architectural	1	3
Payload TRL	Architectural	1	9
Launcher	Architectural	1	15

Table 3 Architectural variables

Type of solar cells	Efficiency	Power density, kg/W
1 Silicon	14.08	115
2 Ga-As	24	140
3 Custom	20	100
Type of batteries	**Energy density, Wh/kg**	
1 Nickel–Cadmium	25	
2 Nickel–Hydrogen	35	
3 Lithium–Ion	140	
Payload TRL		
Affects the cost of the payload for a given performance		
Launcher		
The launchers are selected from the database presented in [40,44]. Affects the mass available for a given orbit and the mission cost.		

Table 4 Most Pareto-robust design-variable settings

Design variable			Most Pareto-robust solution	CCD		
				Low (X_1)	Central point (X_0)	High (X_1)
Eccentricity	[-]	A	0.02	0.02	0.059	0.098
Semimajor axis	[km]	B	8046.9	8046.9	11607.0	15167.0
Inclination	[deg]	C	19.7	10.7	19.7	28.7
Payload aperture diameter	[m]	D	0.997	0.817	0.907	0.997
Satellite transmitters output power (RF power)	[W]	E	1	1	30.9	60
Satellite aperture-antenna diameter	[m]	F	0.1	0.1	0.19	0.28
Telemetry data rate	[Mbps]	G	1.05	1.05	1.25	1.45
Launcher	[-]	H	9	8	9	10
TRL	[-]		9		Frozen	
Type of solar cell	[-]		3		Frozen	
Type of battery	[-]		2		Frozen	

Table 5 Selected design baseline

Design variable			Selected design baseline
Eccentricity	— —	A	0.02
Semimajor axis	km	B	9400.0
Inclination	deg	C	19.7
Payload aperture Diameter	m	D	0.817
Satellite transmitters output power (RF power)	W	E	1
Satellite aperture-antenna diameter	m	F	0.1
Telemetry data rate	Mbps	G	1.25
Launcher	— —	H	8
Cost [M$FY2010]	Coverage [x 100%]	Spatial resolution [m@SSP]	
311	6.5	5.5	